ACS APPLIED MATERIALS & INTERFACES

Research Article

Cite This: ACS Appl. Mater. Interfaces 2019, 11, 44905−44912

www.acsami.org

Breaking Lattice Symmetry in Highly Strained Epitaxial VO_2 Films on Faceted Nanosurface

Yanda Ji,[†] Zhimin Qi,[‡] Shikhar Misra,[‡] Rongqiang Jin,[†] Xin Ou,[§] Yuan Lin,[∥] Hao Yang,*[,†] and Haiyan Wang*[,‡]

[†]Department of Applied Physics, College of Science, Nanjing University of Aeronautics and Astronautics, 211106 Nanjing, P. R. China

[‡]School of Materials Engineering, Purdue University, West Lafayette, Indiana 47907, United States

[§]State Key Laboratory of Functional Material for Informatics, Shanghai Institute of Microsystem and Information Technology, Chinese Academy of Sciences, 200250 Shanghai, P. R. China

[∥]State Key Laboratory of Electronic Thin Films and Integrated Devices, University of Electronic Science and Technology of China, 610054 Chengdu, P. R. China

Supporting Information

ABSTRACT: The lattice symmetry of strongly correlated oxide heterostructures determines their exotic physical properties by coupling the degrees of freedom between lattices and electrons, orbitals, and spin states. Systematic studies on VO_2, a Mott insulator, have previously revealed that lattice distortion can be manipulated by the interfacial strain and electronic phase separation can emerge. However, typical epitaxial film-substrate interface strain provides a very limited range for exploring such interface-engineered phenomena. Herein, epitaxially grown VO_2 thin films on asymmetrically faceted m-plane sapphire substrates with the hill-and-valley type surfaces have been demonstrated. Interestingly, lattice symmetry breaking has been proven based on the large residual strain from the different faceted planes. By this lattice symmetry breaking, electronic phase separation and metal−insulator transition in the VO_2 films are modulated, and anisotropy in optical responses is exhibited. These results on asymmetrical interfacial engineering in oxide heterostructures open up new routes for novel functional materials design and functional electro/optic device nanofabrication.

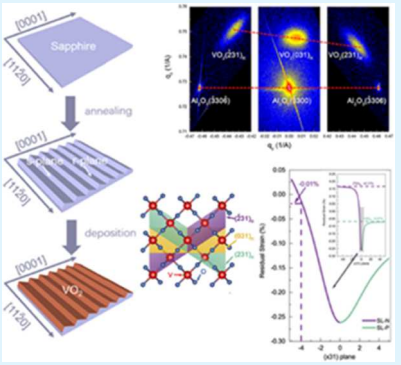

KEYWORDS: *lattice symmetry breaking, vanadium dioxide, epitaxial growth, surface, interfacial engineering*

INTRODUCTION

By breaking the symmetry of space/time inversion, anomalous behaviors can be evoked in strongly correlated materials, including colossal magnetoresistance, ferroelectricity, superconductivity, and metal−insulator transitions (MITs).[1−5] At the same time, interfacial engineering plays a key role in tailoring lattices and critical behaviors in strongly correlated oxide heterostructures. For example, ABO_3 perovskite oxide thin films can be epitaxially grown on orthorhombic substrates such as $NdGaO_3$ or $GdScO_3$ with interface-engineered oxygen octahedral structures to induce anisotropy.[6−8] Additionally, the use of vicinal surfaces formed by substrate miscuts is another practical route for guiding the epitaxial growth of films with anisotropic in-plane strains.[9,10] In addition to these materials, vanadium dioxide (VO_2) is a typical strongly correlated oxide with a 4−5 order-of-magnitude sharp MIT at 341 K that is accompanied by a structural phase transition (SPT) from the low-temperature monoclinic phase to the high-temperature rutile phase.[11−13] VO_2 has been widely researched in the fields of microelectronics, optics, and energy harvesting.[14−16] Interfacial engineering has been used to tune the critical temperature point to room temperature.[17]

Due to the neighboring positions of Ti and V in the periodic table of elements, their atomic radii are very similar. The rutile TiO_2 structure belongs to the same space group ($P42/mnm$ (136)) as the high-temperature phase of VO_2. Therefore, the epitaxial nature of VO_2/TiO_2 can be guaranteed. Until now, the interfacial engineering of VO_2 heterostructures has mainly been performed on TiO_2 substrates. Lu et al. and Kittiwatanakul et al. used TiO_2(011) and TiO_2(001) substrates to grow VO_2 thin films, and anisotropic direct current conductivity induced by interfacial strain was observed.[18,19] The optical responses, including THz transmission and far-IR conductivity, of strained VO_2 films associated with nanoscale electronic phase separation (EPS) during the MIT were reported.[20,21] Recently, Corder et al. demonstrated local strain-induced electronic anisotropy in VO_2 thin films on focused-ion-beam-patterned TiO_2 substrates, demonstrating the feasibility of interfacial nanoengineering of functional strongly correlated materials by introducing nanoscale roughness and

Received: September 11, 2019
Accepted: November 4, 2019
Published: November 18, 2019

DOI: 10.1021/acsami.9b16455
ACS Appl. Mater. Interfaces 2019, 11, 44905−44912

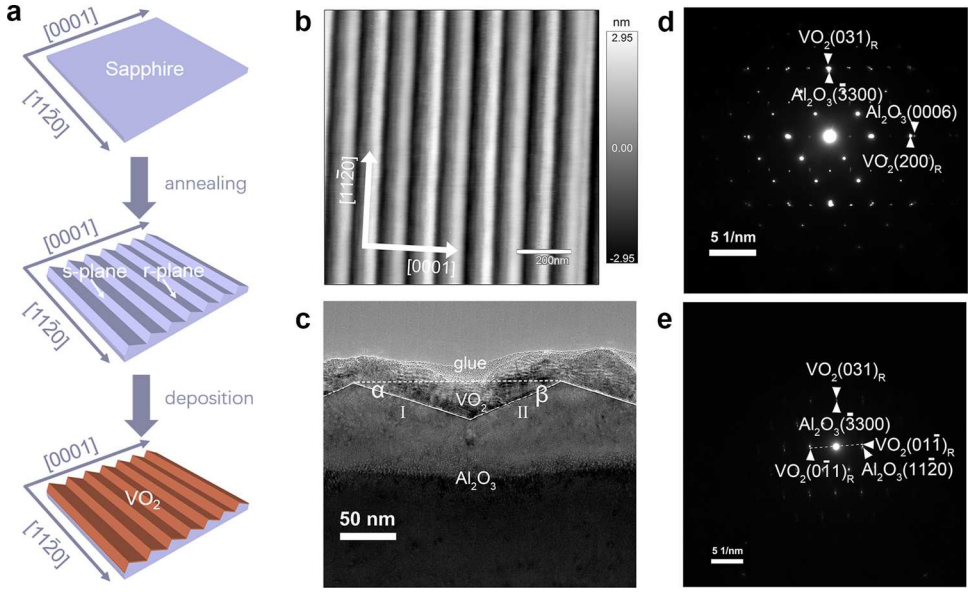

Figure 1. Overview of VO_2 thin films grown on a faceted m-plane sapphire substrate. (a) The schematic diagrams of film fabrication. (b) Top view of the bare substrate surface after annealing, as characterized by atomic force microscopy (AFM). The nanostripes form a hill-and-valley structure along with the direction of the sapphire [11$\bar{2}$0]. (c) Transmission electron microscopy (TEM) images are taken from the sapphire [11$\bar{2}$0] plane. The asymmetric facet planes (I and II) with different axial angles (α, β) from the original m-plane surface are formed. (d, e) Selected area electron diffraction (SAED) results taken from the sapphire [11$\bar{2}$0] (d) and [0001] planes (e). The interfacial relationship between VO_2 and the m-plane sapphire substrate is deduced.

exposure of different substrate facets.[22] Based on these experimental results, TiO_2 can be regarded as a reasonable substrate for VO_2. However, this model is very limited. Developing new substrate surface platforms to explore the integration of novel functionalities into VO_2 heterostructures remains an open question in materials science and nanotechnology research. In this work, we propose to grow VO_2 thin films on asymmetrically faceted m-plane sapphire substrates with the hill-and-valley type surfaces (Figure 1a). The m-plane sapphire surface is metastable and can spontaneously develop the hill-and-valley type surfaces formed by periodic r-planes and s-planes with long-range order by annealing.[23−26] Such unique substrate surfaces have been developed as templates to guide the growth of nanowires.[27−30] Epitaxially grown VO_2 on these asymmetric facet-surfaces can take advantage of various interfacial strain states enabled by this unique asymmetrically faceted substrate surfaces. Moreover, unlike the biaxial strain demonstrated above, novel structures and behaviors of electron/photon interactions under different strain states along a single axis would be expected. Based on the recent epitaxial growth of VO_2 on r-plane sapphire substrates[31,32] and on nonfaceted m-plane sapphire,[33] epitaxial growth of VO_2 on faceted m-plane sapphire is promising. Detailed diffraction and microscopy analyses on the as-grown VO_2 films along with the electrical and optical testing demonstrate the novel strain VO_2 films.

RESULTS AND DISCUSSION

Interfacial Relationship and Breaking the Inversion Symmetry of the VO_2 Lattice. VO_2 heterostructures were fabricated on faceted m-plane sapphire substrates by pulsed laser deposition (PLD). As the atomic force microscopy (AFM) images shown in Figure 1b, one-dimensional (1D) hill-and-valley structures with approximately 10 periods of 1 μm are obtained on the substrates. After deposition, the VO_2 thin films were stabilized by following the substrate surface geometry (Figure 1c). The asymmetric surfaces are obvious on the m-plane sapphire substrate. The wrinkled VO_2 thin film is approximately 30 nm, which is within the empirical critical thickness for interfacial interactions. The axial angle (α) between the original surface and the facet plane I is approximately 17°, and the lattice constant of the perpendicular direction from the surface calculated from the high-resolution transmission electron microscopy (HRTEM) image (see below) is approximately 1.909 Å. The s-plane can be undoubtedly verified. In the same way, the lattice constant normal to the facet plane II is 3.377 Å, which indicates the r-plane. However, the axial angle (β) is approximately 22°, which is far from the theoretical axial angle of 32.4° between the original m-plane and the r-plane of the sapphire substrate. Meanwhile, the discontinuous contrast at the r-plane interface indicates different interactions between the VO_2 film and the asymmetrical surfaces. Based on the selected area electron diffraction (SAED) patterns as shown in Figure 1d,e, the epitaxial growth of the rutile VO_2 films on the faceted m-plane sapphire substrate follows the interfacial relationship of $VO_2(031)_R//Al_2O_3(\bar{3}300)$, $VO_2(100)_R//Al_2O_3(0001)$, and $VO_2(01\bar{1})_R//Al_2O_3(11\bar{2}0)$. For simplicity, the VO_2 rutile lattice indexes are still used for the monoclinic phase, and the conversion is shown in the Supporting Information (Section S1). It should be noted that the in-plane crystal axis of $VO_2[100]_R$ is parallel to that of $Al_2O_3[0001]$, whereas a small crystal angle exists between the $VO_2(01\bar{1})_R$ and in-plane direction of $Al_2O_3[11\bar{2}0]$. To systematically monitor the structural evolution of the asymmetrical epitaxial VO_2 thin films across the intrinsic SPT, we obtained temperature-dependent in situ X-ray diffraction reciprocal space maps (XRD-RSMs). In line with the TEM coordinates, the directions of the sapphire [11$\bar{2}$0], [0001], and [$\bar{1}$100] are defined as the x, y, and z axes, respectively. The 1D geometric nanostripes of the hill-and-valley morphology are exhibited

DOI: 10.1021/acsami.9b16455
ACS Appl. Mater. Interfaces 2019, 11, 44905−44912

along with the *x*-axis. The interfacial effects should be conspicuous along with the *y*-axis. The out-of-plane and in-plane RSMs taken from the *y*-axis of rutile VO_2 at 363 K are shown in Figure 2a. The detailed RSMs for various

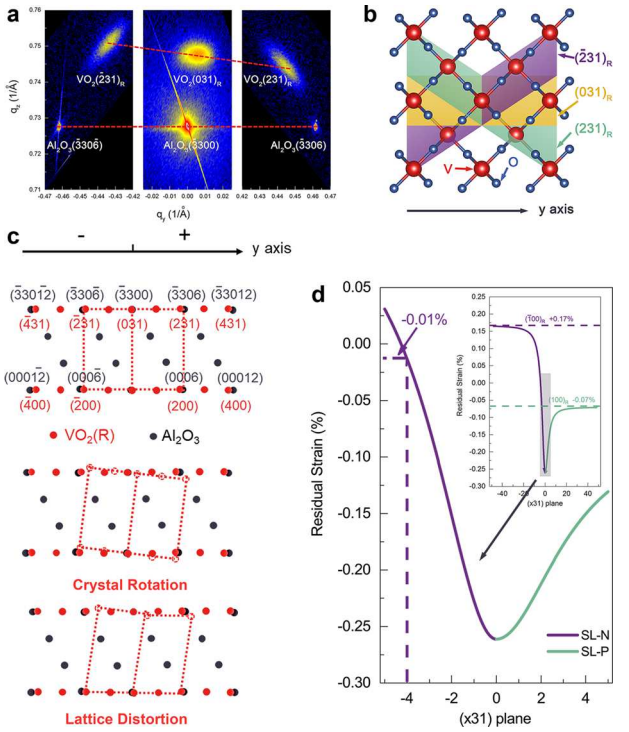

Figure 2. Breakage of the lattice symmetry in rutile VO_2 thin films grown on a faceted m-plane sapphire substrate. (a) At 363 K, XRD-RSMs taken around the sapphire $(\bar{3}30\bar{6})$, $(\bar{3}300)$, and $(\bar{3}306)$ planes. (b) The probed planes in the real space of rutile VO_2. (c) A schematic in reciprocal space to illustrate the asymmetry of VO_2. (d) Numerical computations of SL-N and SL-P residual strain states from the out-of-plane direction to the in-plane $\langle 100\rangle_R$ direction. The inset figure shows the opposite strain states for the VO_2 lattices deduced from the *y*-axis.

temperatures and lattice structures are shown in the Movies S1−S5 and S2 in Supporting Information. Considering the rutile structure of VO_2, the lattice parameter of $VO_2(031)_R$ is 1.3366 Å, and the diffraction spot is 0.44° from out-of-plane direction (theoretical position), which indicate the lattice rotation along the clockwise direction in our measurements. From the asymmetric XRD patterns, the diffraction spots of VO_2 $\{231\}_R$ are recorded to calculate the in-plane lattice constants. It is obvious that the spots do not have phenomenological inversion symmetry. From the negative *y*-axis, which can be treated as a sublattice (SL-N), is a clockwise rotation of approximately 0.55° from the theoretical position, and the lattice constant is 1.1531 Å. From the positive *y*-axis is a clockwise rotation of approximately 0.43° from the theoretical position, and the lattice constant is 1.1538 Å. As shown in Figure 2b,c, this structure can be ascribed to crystal rotation, which cannot affect the lattice constants and crystal lattice distortion. Deducting the clockwise 0.44° crystal rotation reveals the lattice distortion. SL-N eventually shows a clockwise rotation of approximately 0.11°, and the calculated tensile lattice strain along with $VO_2[\bar{1}00]_R$ is 0.17%. Nevertheless, a compressive stain of 0.07% is present along with the $VO_2[100]_R$ of SL-P. Numerical computations of the two sublattice strain values from the out-of-plane direction to the in-plane $\langle 100\rangle_R$ direction are shown in Figure 2d, and breakage of the inversion symmetry of the VO_2 lattice is clearly confirmed.

To unravel the underlying mechanism of VO_2 with broken lattice symmetry, the detailed interfacial interactions should be carefully investigated. According to the epitaxial relationship mentioned above, the lattice matching on the s-planes and r-planes is $VO_2(131)_R//Al_2O_3(\bar{3}303)$ and $VO_2(\bar{2}31)_R//Al_2O_3(\bar{3}30\bar{6})$, respectively. Considering the in-plane interfacial relationship of $VO_2[100]_R//Al_2O_3[0001]$, in theory, the lattice mismatch can reach +5.2%, which can understandably induce compressive strain along with this direction. In the normal epitaxial model, misfit dislocations form at the interface to relieve lattice mismatch during the growth of coherently strained thin films. As the number of misfit dislocations increases, the strain is partially released as the thickness of the film increases until the film is completely relaxed.[34] In low-temperature phases, the theoretical lattice mismatch is still as large as 4.3% along with the sapphire [0001]. The SPT cannot change already-formed misfit dislocations, which is the main mechanism for strain relaxation. Such misfit dislocations are observed at the interface of the s-planes in the HRTEM image (Figure 3a). As a result, the residual compressive strain of 0.07% is reasonable and indicates that SL-P should be stabilized on the s-planes.

Because SL-N and SL-P follow the same interfacial relationship, the completely opposite strain states of $[100]_R$ in SL-N cannot be understood using the above epitaxial model. In fact, surface step terraces (SSTs) are present on the r-planes (Figure 3b). Chen et al. developed a model for inducing local strain by lattice mismatch on step terraces that may explain the origin of the strain in SL-N.[35−38] In theory, the local strain ε induced by SSTs can be calculated as follows[39,40]

$$\Delta d = D - N_f a_f \tag{1}$$

$$a'_f = a_f + \frac{\Delta d}{N_f a_f} \tag{2}$$

$$a'_f = a_f + \frac{\Delta d - a_f}{(N_f + 1)a_f} \tag{3}$$

$$\varepsilon = \frac{(a'_f - a_f)}{a_f} \tag{4}$$

where Δd is the residual space, D is the width of the terrace, N_f is the maximum number of film unit cells on one terrace to ensure positive Δd, a_f is the lattice constant of the bulk film, and a_f' is the resultant unit-cell spacing in the film. Equation 2 is for elongated conditions, and eq 3 is for the compressed case.

The HRTEM results show that the step terraces are formed by the $(\bar{1}10\bar{2})$ planes (r-planes) and $(\bar{1}104)$ planes. We filtered the images of the two planes by inverse fast Fourier transformations (IFFTs) (Figure 3c,d). By fitting the structural parameters of the five observed step terraces, the average characteristic angle (γ) of 10.0° is obtained, which agrees with the different values of the β axis in Figure 1c. In this case, the width of the SSTs should be 15 times the lattice constant of $Al_2O_3(\bar{1}104)$ (38.26 Å) (Supporting Information Section S3). It should be noted that 1 unit-cell of VO_2 contains four times the lattice constant of $(431)_R$ (Supporting Information Section S4). If 11 VO_2 unit cells are stabilized on each SST, the lattice

DOI: 10.1021/acsami.9b16455
ACS Appl. Mater. Interfaces 2019, 11, 44905−44912

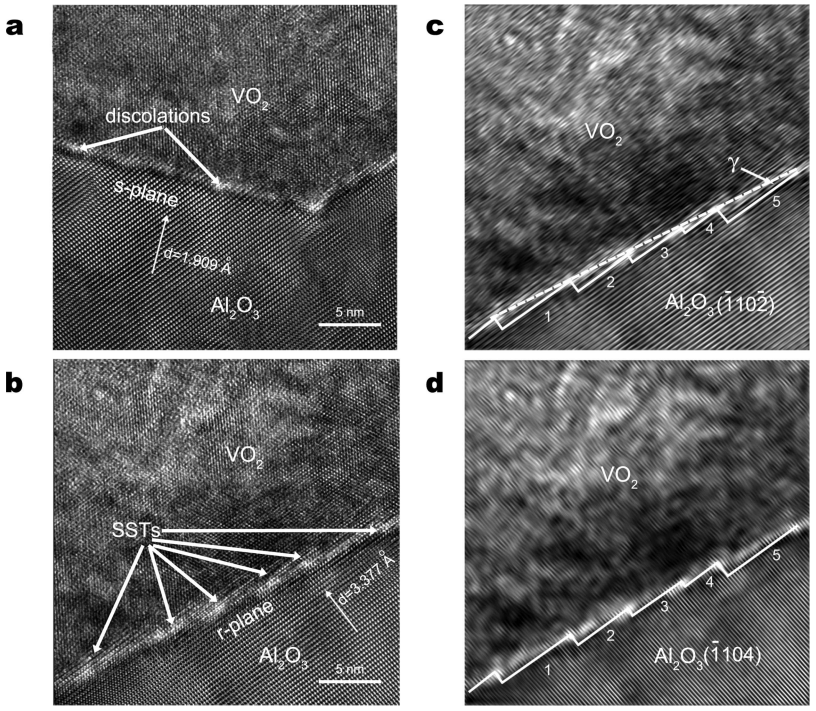

Figure 3. Interfacial interactions of VO_2 thin films grown on faceted m-plane sapphire substrates. (a) HRTEM images taken from the faceted s-plane; the interfacial dislocations suggest the films grown on s-planes follow the normal epitaxial model. (b) The SST structures in HRTEM images taken from the faceted r-plane. (c, d) HRTEM image filtered by inverse fast Fourier transforms (FFTs) for SST modeling; $Al_2O_3(\bar{1}102)$ planes are in (c), and $Al_2O_3(\bar{1}104)$ planes are in (d).

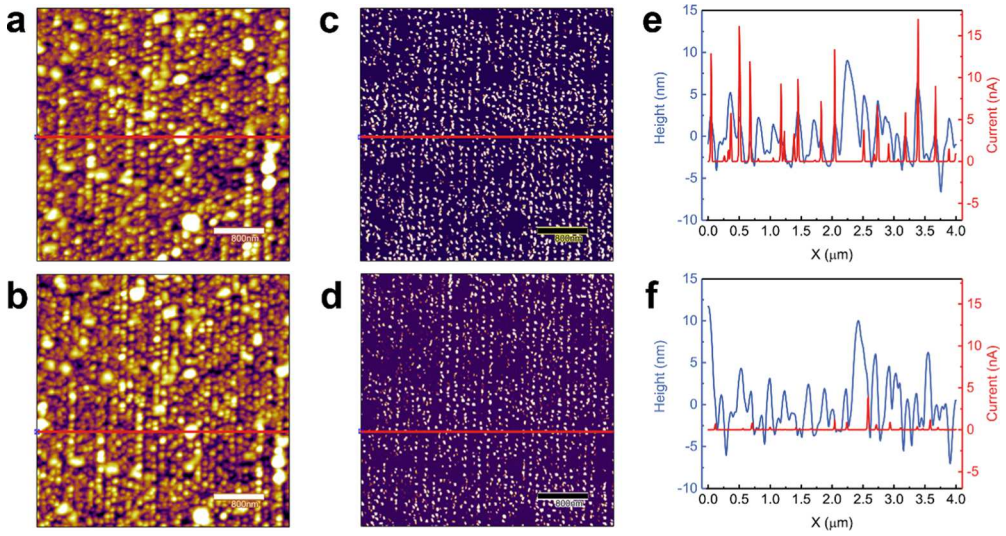

Figure 4. Statues of EPS during the cooling process. (a, b) AFM images were taken at 365 K (a) and 325 K (b). (c, d) The corresponding C-AFM images of 365 K (c) and 325 K (d). (e, f) The profile of the red line in each image including the signals of the height and current that are shown at 365 K (e) and 325 K (f). During the cooling process, the peaks from the current shift from the peaks to the falling edges of the VO_2 surface.

mismatch should be −0.21%. In Figure 2d, the strain for $(\bar{4}31)_R$ could be negligible in SL-N with such a small mismatch. These results are consistent with the fact that SL-N is governed by SSTs on r-planes.

Electronic Phase Separations and Metal−Insulator Transitions Influenced by Broken Lattice Symmetry. X-ray absorption spectroscopy results by Parkin et al. revealed that the strain along with $VO_2[110]_R$ manipulates the molecular orbitals, which modulate the electronic transport properties.[34] Phenomenologically, the MIT critical transition point (T_{MIT}) and conductivity can be tuned by the lattice constant ratio of c_R/a_R. In our films, different c_R/a_R can be deduced: 0.628 for SL-N and 0.629 for SL-P. In this case, a lower T_{MIT} can be expected for SL-N than SL-P. Conductive atomic force microscopy (C-AFM) measurements were performed during a cooling process from 365 to 325 K (Supporting Information Section S5).[41] As shown in Figure 4, at a high temperature (365 K), the high conductance areas are focused on the peak morphology, which indicates the metallic-phase VO_2 on both sapphire s-planes and r-planes results in simultaneous conductance. As the temperature decreases, the transition of the VO_2 on the rising edges of the hill-and-valley

DOI: 10.1021/acsami.9b16455
ACS Appl. Mater. Interfaces 2019, 11, 44905−44912

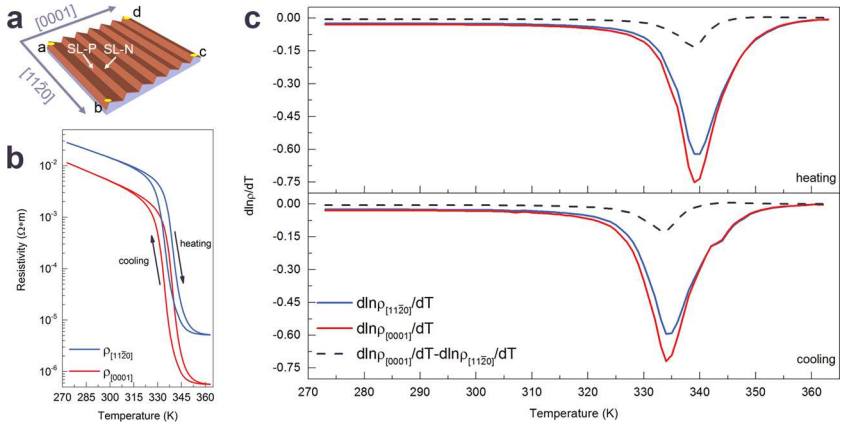

Figure 5. Metal−insulator transitions of the VO_2 thin films. (a) The schematic diagram of Van der Pauw geometry. (b) Resistivity versus temperature curves along with different in-plane directions. (c) The differential curves of $\ln\rho$ versus temperature along with each in-plane directions.

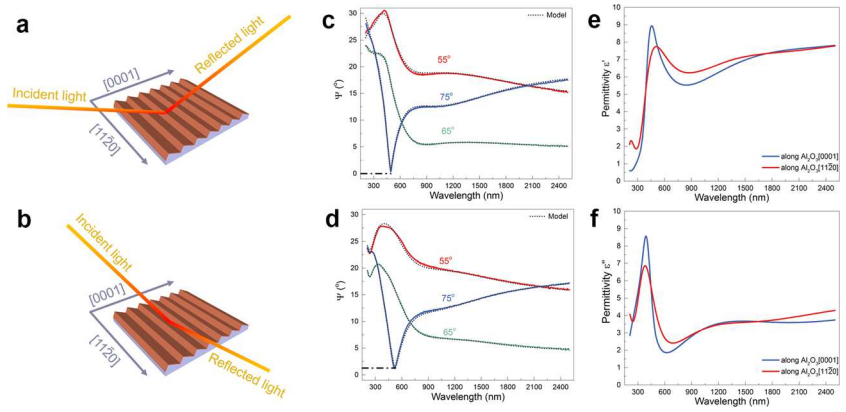

Figure 6. Optical properties of the VO_2 thin films. (a, b) Schematic diagram for the incidence of light along with sapphire [0001] and [11$\bar{2}$0], respectively. (c, d) Ellipsometric parameter Ψ measured at 55, 65, and 75°, versus wavelength along with in-plane directions of [0001] (c) and [11$\bar{2}$0] (d). (e, f), Real part (ε') and imaginary part (ε'') of the dielectric permittivity fitted for the incident light along with [0001] (blue) and [11$\bar{2}$0] (red).

structure to the insulating phase is faster than that of the VO_2 on the falling edges with a higher T_{MIT}. Then, the current prefers to travel through the part on the falling edges; in this case, the conductance areas are on the falling edges of the substrate. These EPS results provide strong evidence for the different T_{MIT} values for VO_2 films with broken lattice symmetry: SL-N may stabilize on the falling edges, and SL-P may stabilize on the rising edges of the morphology.

According to the EPS results, periodic SL-N and SL-P on the nanofaceted surface should induce different MIT behaviors along with in-plane directions. Phenomenologically, the MIT in VO_2 can be exhibited as a hysteresis loop in the $\ln\rho$ versus temperature curves. In more detail, differential curves of $\ln\rho$ versus temperature can be applied for studying the process. The in-plane film resistivity is calculated by Price's extension to the Van der Pauw method.[42,43] As shown in Figure 5, MIT behavior with an additional transition can be observed along with sapphire [0001], other than along with sapphire [11$\bar{2}$0], in both heating and cooling processes. Along with sapphire [0001], the current should pass through both SL-N and SL-P. As a result, MIT in both of them can be recorded. Along with sapphire [11$\bar{2}$0], the current tends to travel through the low resistance lattices (SL-N). Therefore, part of the MIT information from the high resistance lattices (SL-P) is missing. Finally, the missing MIT from SL-P can be revealed by the difference in the differential curves.

Optical Responses Influenced by Broken Lattice Symmetry. At room temperature, the VO_2 is the monoclinic insulator phase, which is under biaxial optical symmetry with three different dielectric tensors. In other words, in-plane orientation-dependent optical responses should be conspicuous in our epitaxial films. To demonstrate the effects, linearly polarized light was incident onto the VO_2 sample along with in-plane directions of sapphire [0001] and sapphire [11$\bar{2}$0], respectively. The reflected light is collected for further analysis.[44] Because of the different reflection coefficients for the s-polarized and p-polarized components of the incident light, the amplitude and phase would change after reflection. In Figure 6, the ellipsometric angles under various wavelengths are measured with the light incident angle of 55, 65, and 75°, respectively. The substrate was backside roughened to minimize the reflection from the back surface. In the case of incidence along with sapphire [0001], the light travels through the SL-N and SL-P in series (Figure 6a), multifiltration at the interfaces would be expected. While, in the case of incidence along with sapphire [11$\bar{2}$0], the light goes across the SL-N and SL-P in parallel (Figure 6b), being reflected without the interface filtration. This leads to the obvious difference in the Ψ (Figure 5c,d) and Δ (Section S6 in Supporting Information)

DOI: 10.1021/acsami.9b16455
ACS Appl. Mater. Interfaces 2019, 11, 44905−44912

ellipsometer parameters since the reflection geometry is different for the two cases. When the light is incident along with sapphire [0001], the Ψ value decreases to 0, while a sharp change can be seen in the phase shift (Δ) curve at 75° incident angle. However, for the case of light propagating along with sapphire [11$\bar{2}$0], the Ψ value do not reach 0 and the degrees and sharpness of phase shift (Δ) are weaker than that case of incidence along with sapphire [0001] at 75° incident angle. As a result, the ellipsometer parameters, Ψ and Δ, are in-plane orientation-dependent. Such a phenomenon may be understood by the broken lattice symmetry. In principle, the optical constants are strongly coupled to strain states in crystal films. Therefore, the dielectric permittivity of SL-N and SL-P would be obtained with a small difference. The real and imaginary parts of permittivity were modeled using an isotropic general oscillator model to enforce Kramers−Kronig consistency, and are plotted in Figure 6e,f, respectively. Clearly, the permittivity along with the sapphire [0001] and [11$\bar{2}$0] are different, arising possibly due to the in-plane anisotropy.

CONCLUSIONS

In summary, VO_2 with broken lattice symmetry has been achieved by epitaxial growth VO_2 on asymmetric nanofaceted m-plane sapphire substrates with s-planes and r-planes as the nanofacets. On the s-planes, the film growth follows a normal epitaxial model. On the r-planes, surface step terraces are obtained and additional local strain is introduced into the film to induce breakage of the lattice symmetry. The phenomenological electronic phase separation is also probed, and the results indicate that different critical MIT points are present in films with broken lattice symmetry. The MIT behaviors and optical responses of the film are proved to be modulated by the surface structures. Compared to traditional anisotropy induced by biaxial elastic strain, we have realized a new route to stabilize different strain states along a single axis in crystalline films, which not only expands the fundamental understanding of the crystallography of heterostructure growth but also provides a new path for manipulating the functionality of materials and devices enabled by nanosurface engineering.

METHODS

Sample Preparation. The m-plane sapphire substrates were ultrasonically cleaned in sequence by alcohol, acetone, and isopropanol. Then, the cleaned substrates were placed into a furnace, heated to 1673 K at a rate of 10 K/min, and kept at the maximum temperature for 16 h. Then, the substrates were cooled to room temperature at a rate of 5 K/min. The VO_2 thin films were deposited by pulsed laser deposition (PLD-300 from SKY Technology Development Co., Ltd., CAS). The polycrystalline vanadium sesquioxide (V_2O_3) target was purchased from Hefei Kejing Materials Technology Co., Ltd. The laser energy density was 1.6 J/cm^2 with a repetition rate of 2 Hz, and the distance between the target and substrate was approximately 60 mm. During the growth process, the temperature was constant at 903 K, and the O_2 atmosphere remained at 1.33 Pa.

Structure Characterization. XRD was performed by using a Panalytical Empyrean diffractometer. The X-ray was radiated from the copper target with a wavelength of 1.54059 Å, and the highly collimated Kα1 beam was filtered by a commercial Ge(220) hybrid monochromator. The detector was a PIXcel 1D detector with 256 matrix channels and the resolution of each channel was 55 μm. The temperature was controlled by a Domed Hot Sstage with four-circle goniometers (Anton-paar, DHS 1100). TEM images and SAED patterns were taken by an FEI TALOS 200X instrument. The samples were thinned by cutting and manual grinding at first and then by dimpling and ion polishing with a precision polishing system (PIPS II).

SPM Measurement. The AFM and C-AFM measurements were simultaneously carried out by the Asylum Research MFP-3D system equipped with an ocra module. The FM-LC tip was obtained from Adama. During the measurements, only a 50 mV voltage was applied to the tip to avoid Joule heating.

Resistance Measurement. The resistance was measured by Keysight B2902A. The four wires were connected to each corner of the squared samples mounted by silver paste according to the Van der Pauw method. The temperature was controlled by Linkam THMS600. At each temperature, the resistance was measured using a current and reversed current of 50 μA, and the final value was the average of them. The resistance along with different orientations was synchronously recorded under the remaining temperature. The Price's extension to the Van der Pauw method is for calculating the anisotropy in resistance, as below[42,43]

$$\exp\left(-\frac{\pi d}{\rho_{iso}}R_{ab,cd}\right)+\exp\left(-\frac{\pi d}{\rho_{iso}}R_{ad,cb}\right)=1 \tag{5}$$

$$\rho_{iso}=\sqrt{\rho_x\rho_y} \tag{6}$$

$$\sqrt{\frac{\rho_x}{\rho_y}}=-\frac{1}{\pi}\ln\left(\tanh\left[\frac{\pi d R_{ad,cb}}{16\rho_{iso}}\right]\right) \tag{7}$$

$$\rho_x=\rho_{iso}\left(\sqrt{\frac{\rho_x}{\rho_y}}\right) \tag{8}$$

$$\rho_y=\rho_{iso}/\left(\sqrt{\frac{\rho_x}{\rho_y}}\right) \tag{9}$$

where d is the thickness of the films and R is the measured resistance (Section S5 in Supporting Information). The ρ_{iso} values are numerically computed by classical dichotomy. The ab edge of the squared sample is along with the x-direction and the ad edge of the squared sample is along with the y-direction.

Spectroscopic Ellipsometry. The dielectric permittivity of the samples was calculated using spectroscopic ellipsometry (JA Woollam RC2). The ellipsometer parameters, Ψ and Δ, are used to describe the reflected light[44]

$$\frac{r_p}{r_s}=\tan\Psi\, e^{i\Delta} \tag{10}$$

$$\Delta=\delta_p-\delta_s \tag{11}$$

$$\delta_p=\frac{4\pi d}{\lambda}\frac{n_{1x}}{n_{1z}}\sqrt{n_{1z}^2-n_0^2\sin^2\varphi_0} \tag{12}$$

$$\delta_s=\frac{4\pi d}{\lambda}\sqrt{n_{1y}^2-n_0^2\sin^2\varphi_0} \tag{13}$$

where r_p and r_s are reflection coefficient of p and s-polarized light. δ_p and δ_s are the phase shifts of the p and s components of the light after reflection. d is the film thickness. λ is the wavelength of the incident light. n_{1x}, n_{1y}, and n_{1z} are the refractive indexes of the thin film. X-direction is the light propagation direction, y-direction is along the vibration direction of s polarized light, and z-direction is along the vibration direction of p-polarized light. n_0 is the refractive index of air, and φ_0 is the incident angle. The sample was modeled using two Gaussian, one Lorentz, and one Tauc−Lorentz oscillator. Mean squared error of all the fits was around five.

DOI: 10.1021/acsami.9b16455
ACS Appl. Mater. Interfaces 2019, 11, 44905−44912

■ ASSOCIATED CONTENT

Supporting Information

The Supporting Information is available free of charge on the ACS Publications website at DOI: 10.1021/acsami.9b16455.

Transformation relation of rutile and monoclinic unit cells in VO_2 (Section S1); calculated lattice parameters for SL-P and SL-N (Section S2); modeling for SSTs (Section S3); lattice of Rutile VO_2 (Section S4); electric behaviors of VO_2 thin films (Section S5); more results of spectroscopic ellipsometry (Section S6) (PDF)

Video of in-plane RSMs at various temperatures taken from negative *y*-axis (Movie S1) (MP4)

Video of out-of-plane RSMs at various temperatures taken from *y*-axis (Movie S2) (MP4)

Video of in-plane RSMs at various temperatures taken from positive *y*-axis (Movie S3) (MP4)

Video of out-of-plane RSMs at various temperatures taken from *x*-axis (Movie S4) (MP4)

Video of in-plane RSMs at various temperatures taken from *x*-axis (Movie S5) (MP4)

■ AUTHOR INFORMATION

Corresponding Authors

*E-mail: yanghao@nuaa.edu.cn (H.Y.).
*E-mail: hwang00@purdue.edu (H.W.).

ORCID

Xin Ou: 0000-0002-0316-9958
Yuan Lin: 0000-0002-9879-4341
Hao Yang: 0000-0002-9055-7165
Haiyan Wang: 0000-0002-7397-1209

Author Contributions

Y.J., X.O., Y. L., H.Y., and H.W. discussed and initiated the study, and H.Y. and H.W. supervised the project. Y.J. and R.J. conducted the fabrication experiments and electric measurements. Y.J. performed the XRD and SPM measurements. Z.Q. and H.W. performed the TEM measurements. S.M. conducted spectroscopic ellipsometry under the supervision of H.W., Y.J., Z.Q., S.M., X.O., Y.L., H.W., and H.Y. analyzed the data and cowrote the manuscript. All authors reviewed and finalized the manuscript.

Notes

The authors declare no competing financial interest.

■ ACKNOWLEDGMENTS

We would like to thank Dr Ren Zhu from the AR Demo Lab of Oxford Instruments Technology (Shanghai) Co., LTD. for his technical support of the C-AFM work. This work was supported by the National Natural Science Foundation of China (NSFC, Nos 51602152, U1632122, 11774172, 61874128, 61851406, 11622545, and 61825102). Z.Q., S.M., and H.W. acknowledge the support from the U.S. National Science Foundation (DMR-1809520) for the work at Purdue University.

■ REFERENCES

(1) Zubko, P.; Gariglio, S.; Gabay, M.; Ghosez, P.; Triscone, J. M. Interface Physics in Complex Oxide Heterostructures. *Annu. Rev. Condens. Matter Phys.* **2011**, *2*, 141−165.

(2) Kim, H. J.; Kim, K. S.; Wang, J. F.; Sasaki, M.; Satoh, N.; Ohnishi, A.; Kitaura, M.; Yang, M.; Li, L. Dirac versus Weyl Fermions in Topological Insulators: Adler-Bell-Jackiw Anomaly in Transport Phenomena. *Phys. Rev. Lett.* **2013**, *111*, No. 246603.

(3) Shi, P.-P.; Tang, Y.-Y.; Li, P.-F.; Liao, W.-Q.; Wang, Z.-X.; Ye, Q.; Xiong, R.-G. Symmetry Breaking in Molecular Ferroelectrics. *Chem. Soc. Rev.* **2016**, *45*, 3811−3827.

(4) Mackenzie, A. P.; Maeno, Y. The Superconductivity of Sr_2RuO_4 and the Physics of Spin-triplet Pairing. *Rev. Mod. Phys.* **2003**, *75*, 657−712.

(5) Bert, J. A.; Kalisky, B.; Bell, C.; Kim, M.; Hikita, Y.; Hwang, H. Y.; Moler, K. A. Direct Imaging of the Coexistence of Ferromagnetism and Superconductivity at the $LaAlO_3/SrTiO_3$ Interface. *Nat. Phys.* **2011**, *7*, 767−771.

(6) Ward, T. Z.; Budai, J. D.; Gai, Z.; Tischler, J. Z.; Yin, L. F.; Shen, J. Elastically Driven Anisotropic Percolation in Electronic Phase-Separated Manganites. *Nat. Phys.* **2009**, *5*, 885−888.

(7) Liao, Z.; Huijben, M.; Zhong, Z.; Gauquelin, N.; Macke, S.; Green, R. J.; Aert, S. V.; Verbeeck, J.; Tendeloo, G. V.; Held, K. Controlled Lateral Anisotropy in Correlated Manganite Heterostructures by Interface-Engineered Oxygen Octahedral Coupling. *Nat. Mater.* **2016**, *15*, 425−431.

(8) Kan, D.; Aso, R.; Sato, R.; Haruta, M.; Kurata, H.; Shimakawa, Y. Tuning Magnetic Anisotropy by Interfacially Engineering the Oxygen Coordination Environment in a Transition Metal Oxide. *Nat. Mater.* **2016**, *15*, 432−437.

(9) Yao, G.; Ji, Y.; Liang, W.; Gao, M.; Zheng, S.; Wang, Y.; Li, H.; Wang, Z.; Chen, C.; Lin, Y. Influence of the Vicinal Surface on the Anisotropic Dielectric Properties of Highly Epitaxial $Ba_{0.7}Sr_{0.3}TiO_3$ Thin Films. *Nanoscale* **2017**, *9*, 3068−3078.

(10) Ma, C.; Liu, M.; Collins, G.; Wang, H.; Bao, S.; Xu, X.; Enriquez, E.; Chen, C.; Lin, Y.; Whangbo, M.-H. Magnetic and Electrical Transport Properties of $LaBaCo_2O_{5.5+delta}$ Thin Films on Vicinal(001) $SrTiO_3$ Surfaces. *ACS Appl. Mater. Interfaces* **2013**, *5*, 451−455.

(11) Morin, F. J. Oxides Which Show a Metal-to-Insulator Transition at the Neel Temperature. *Phys. Rev. Lett.* **1959**, *3*, 34−36.

(12) Ji, Y. D.; Pan, T. S.; Bi, Z.; Liang, W. Z.; Zhang, Y.; Zeng, H. Z.; Wen, Q. Y.; Zhang, H. W.; Chen, C. L.; Jia, Q. X.; Lin, Y. Epitaxial Growth and Metal-Insulator Transition of Vanadium Oxide Thin Films with Controllable Phases. *Appl. Phys. Lett.* **2012**, *101*, No. 071902.

(13) Ji, Y.; Zhang, Y.; Gao, M.; Yuan, Z.; Xia, Y.; Jin, C.; Tao, B.; Chen, C.; Jia, Q.; Lin, Y. Role of Microstructures on the M1-M2 Phase Transition in Epitaxial VO_2 Thin Films. *Sci. Rep.* **2014**, *4*, No. 4854.

(14) Yang, Z.; Ko, C.; Ramanathan, S. Oxide Electronics Utilizing Ultrafast Metal-Insulator Transitions. *Annu. Rev. Mater. Res.* **2011**, *41*, 337−367.

(15) Folland, T. G.; Fali, A.; White, S. T.; Matson, J. R.; Liu, S.; Aghamiri, N. A.; Edgar, J. H.; Haglund, R. F.; Abate, Y.; Caldwell, J. D. Reconfigurable Infrared Hyperbolic Metasurfaces Using Phase Change Materials. *Nat. Commun.* **2018**, *9*, No. 4371.

(16) Yi, W.; Tsang, K. K.; Lam, S. K.; Bai, X. W.; Crowell, J. A.; Flores, E. A. Biological Plausibility and Stochasticity in Scalable VO_2 Active Memristor Neurons. *Nat. Commun.* **2018**, *9*, No. 104661.

(17) Lee, D.; Lee, J.; Song, K.; Xue, F.; Choi, S. Y.; Ma, Y. J.; Podkaminer, J.; Liu, D.; Liu, S. C.; Chung, B.; Fan, W. J.; Cho, S. J.; Zhou, W. D.; Lee, J.; Chen, L. Q.; Oh, S. H.; Ma, Z. Q.; Eom, C. B. Sharpened VO_2 Phase Transition via Controlled Release of Epitaxial Strain. *Nano Lett.* **2017**, *17*, 5614−5619.

(18) Lu, J.; West, K. G.; Wolf, S. A. Very Large Anisotropy in the DC Conductivity of Epitaxial VO_2 Thin Films Grown on (011) Rutile TiO_2 Substrates. *Appl. Phys. Lett.* **2008**, *93*, No. 205118.

(19) Kittiwatanakul, S.; Lu, J.; Wolf, S. A. Transport Anisotropy of Epitaxial VO_2 Films near the Metal−Semiconductor Transition. *Appl. Phys. Express* **2013**, *4*, 544−548.

(20) Abreu, E.; Liu, M.; Lu, J.; West, K. G.; Kittiwatanakul, S.; Yin, W.; Wolf, S. A.; Averitt, R. D. THz Spectroscopy of VO_2 Epitaxial Films: Controlling the Anisotropic Properties through Strain Engineering. *New J. Phys.* **2012**, *14*, 1−5.

DOI: 10.1021/acsami.9b16455
ACS Appl. Mater. Interfaces 2019, 11, 44905−44912

(21) Liu, M. K.; Wagner, M.; Abreu, E.; Kittiwatanakul, S.; Mcleod, A.; Fei, Z.; Goldflam, M.; Dai, S.; Fogler, M. M.; Lu, J. Anisotropic Electronic State via Spontaneous Phase Separation in Strained Vanadium Dioxide Films. *Phys. Rev. Lett.* **2013**, *111*, No. 096602.
(22) Corder, S. N. G.; Jiang, J. J.; Chen, X. Z.; Kittiwatanakul, S.; Tung, I. C.; Zhu, Y.; Zhang, J. W.; Bechtel, H. A.; Martin, M. C.; Carr, G. L.; Lu, J. W.; Wolf, S. A.; Wen, H. D.; Tao, T. H.; Liu, M. K. Controlling Phase Separation in Vanadium Dioxide Thin Films via Substrate Engineering. *Phys. Rev. B* **2017**, *96*, No. 161110.
(23) Shchukin, V. A.; Bimberg, D. Spontaneous Ordering of Nanostructures on Crystal Surfaces. *Rev. Mod. Phys.* **1999**, *71*, 1125−1171.
(24) Gabai, R.; Ismach, A.; Joselevich, E. Nanofacet lithography: A New Bottom-Up Approach to Nanopatterning and Nanofabrication by Soft Replication of Spontaneously Faceted Crystal Surfaces. *Adv. Mater.* **2007**, *19*, 1325−1330.
(25) Heffelfinger, J. R.; Bench, M. W.; Carter, C. B. On the Faceting of Ceramic Surfaces. *Surf. Sci.* **1995**, *343*, L1161−L1166.
(26) Heffelfinger, J. R.; Carter, C. B. Mechanisms of Surface Faceting and Coarsening. *Surf. Sci.* **1997**, *389*, 188−200.
(27) Oksenberg, E.; Sanders, E.; Popovitz-Biro, R.; Houben, L.; Joselevich, E. Surface-Guided $CsPbBr_3$ Perovskite Nanowires on Flat and Sapphire with Size-Dependent Photoluminescence and Fast Photoconductive Response. *Nano Lett.* **2018**, *18*, 424−433.
(28) Ismach, A.; Kantorovich, D.; Joselevich, E. Carbon Nanotube Graphoepitaxy: Highly Oriented Growth by Faceted Nanosteps. *J. Am. Chem. Soc.* **2005**, *127*, 11554−11555.
(29) Tsivion, D.; Schvartzman, M.; Popovitz-Biro, R.; Joselevich, E. Guided Growth of Horizontal ZnO Nanowires with Controlled Orientations on Flat and Sapphire Surfaces. *ACS Nano* **2012**, *6*, 6433−6445.
(30) Rothman, A.; Forsht, T.; Danieli, Y.; Popovitz-Biro, R.; Rechav, K.; Houben, L.; Joselevich, E. Guided Growth of Horizontal ZnS Nanowires on Flat and Sapphire Surfaces. *J. Phys. Chem. C* **2018**, *122*, 12413−12420.
(31) Garry, G.; Durand, O.; Lordereau, A. Structural, Electrical and Optical Properties of Pulsed Laser Deposited VO_2 Thin Films on R- and C-Sapphire Planes. *Thin Solid Films* **2004**, *453*−*454*, 427−430.
(32) Zhao, Y.; Lee, J. H.; Zhu, Y.; Nazari, M.; Chen, C.; Wang, H.; Bernussi, A.; Holtz, M.; Fan, Z. Structural, Electrical, and Terahertz Transmission Properties of VO_2 Thin Films Grown on C-, R-, and M-Plane Sapphire Substrates. *J. Appl. Phys.* **2012**, *111*, No. 053533.
(33) Feng, J.; Yang, C.; Zhang, A.; Li, Q.; Fan, Z.; Qin, M.; Zeng, M.; Gao, X.; Lin, Y.; Zhou, G.; Lu, X.; Liu, J.-M. Direct Evidence for the Coexistence of Nanoscale High-Conduction and Low-Conduction Phases in VO_2 Films. *Appl. Phys. Lett.* **2018**, *113*, No. 173104.
(34) Aetukuri, N. B.; Gray, A. X.; Drouard, M.; Cossale, M.; Gao, L.; Reid, A. H.; Kukreja, R.; Ohldag, H.; Jenkins, C. A.; Arenholz, E.; Parkin, S. S. P. Control of the Metal-Insulator Transition in Vanadium Dioxide by Modifying Orbital Occupancy. *Nat. Phys.* **2013**, *9*, 661−666.
(35) Lin, Y.; Chen, C. L. Interface Effects on Highly Epitaxial Ferroelectric Thin Films. *J. Mater. Sci.* **2009**, *44*, 5274−5287.
(36) Yao, G.; Gao, M.; Ji, Y.; Liang, W.; Gao, L.; Zheng, S.; Wang, Y.; Pang, B.; Chen, Y. B.; Zeng, H.; Li, H.; Wang, Z.; Liu, J.; Chen, C.; Lin, Y. Surface Step Terrace Tuned Microstructures and Dielectric Properties of Highly Epitaxial $CaCu_3Ti_4O_{12}$ Thin Films on Vicinal $LaAlO_3$ Substrates. *Sci. Rep.* **2016**, *6*, No. 34683.
(37) Jiang, J. C.; Lin, Y.; Chen, C. L.; Chu, C. W.; Meletis, E. I. Microstructures and Surface Step-Induced Antiphase Boundaries in Epitaxial Ferroelectric $Ba_{0.6}Sr_{0.4}TiO_3$ Thin Film on MgO. *J. Appl. Phys.* **2002**, *91*, 3188−3192.
(38) Zou, Q.; Liu, M.; Wang, G. Q.; Lu, H. L.; Yang, T. Z.; Guo, H. M.; Ma, C. R.; Xu, X.; Zhang, M. H.; Jiang, J. C.; Meletis, E. I.; Lin, Y.; Gao, H. J.; Chen, C. L. Step Terrace Tuned Anisotropic Transport Properties of Highly Epitaxial $LaBaCo_2O_{5.5+delta}$ Thin Films on Vicinal $SrTiO_3$ Substrates. *ACS Appl. Mater. Interfaces* **2014**, *6*, 6704−6708.
(39) Lu, H.; Zhang, C.; Guo, H.; Gao, H.; Liu, M.; Liu, J.; Collins, G.; Chen, C. Surface-Step-Terrace-Induced Anomalous Transport Properties in Highly Epitaxial $La_{0.67}Ca_{0.33}MnO_3$ Thin Films. *ACS Appl. Mater. Interfaces* **2010**, *2*, 2496−2499.
(40) Ma, C.; Liu, M.; Chen, C.; Lin, Y.; Li, Y.; Horwitz, J. S.; Jiang, J.; Meletis, E. I.; Zhang, Q. The Origin of Local Strain in Highly Epitaxial Oxide Thin Films. *Sci. Rep.* **2013**, *3*, No. 3092.
(41) Preziosi, D.; Lopez-Mir, L.; Li, X.; Cornelissen, T.; Lee, J. H.; Trier, F.; Bouzehouane, K.; Valencia, S.; Gloter, A.; Barthélémy, A.; Bibes, M. Direct Mapping of Phase Separation across the Metal−Insulator Transition of $NdNiO_3$. *Nano Lett.* **2018**, *18*, 2226−2232.
(42) Kateb, M.; Jacobsen, E.; Ingvarsson, S. Application of an Extended Van Der Pauw Method to Anisotropic Magnetoresistance Measurements of Ferromagnetic Films. *J. Phys. D: Appl. Phys.* **2019**, *52*, No. 075002.
(43) Price, W. L. V. Electric Potential and Current Distribution in a Rectangular sample of Anisotropic Material with Application to the Measurement of the Principal Resistivities by an Extension of Van Der Pauw's Method. *Solid-State Electron.* **1973**, *16*, 753−762.
(44) Tompkins, H. G.; Irene, E. A. *Handbook of Ellipsometry*, William Andrew, Inc., 2005.

DOI: 10.1021/acsami.9b16455
ACS Appl. Mater. Interfaces 2019, 11, 44905−44912